

SHORT REPORT

The molecular architecture of hemidesmosomes, as revealed with super-resolution microscopy

Leila Nahidiazar¹, Maaïke Kreft¹, Bram van den Broek¹, Pablo Secades¹, Erik M. M. Manders^{1,2}, Arnoud Sonnenberg^{1,*} and Kees Jalink^{1,*}

ABSTRACT

Hemidesmosomes have been extensively studied with immunofluorescence microscopy, but owing to its limited resolution, the precise organization of hemidesmosomes remains poorly understood. We studied hemidesmosome organization in cultured keratinocytes with two- and three-color super-resolution microscopy. We observed that, in the cell periphery, nascent hemidesmosomes are associated with individual keratin filaments and that $\beta 4$ integrin (also known as ITGB4) is distributed along, rather than under, keratin filaments. By applying innovative methods to quantify molecular distances, we demonstrate that the hemidesmosomal plaque protein plectin interacts simultaneously and asymmetrically with $\beta 4$ integrin and keratin. Furthermore, we show that BP180 (BPAG2, also known as collagen XVII) and BP230 (BPAG1e, an epithelial splice variant of dystonin) are characteristically arranged within hemidesmosomes with BP180 surrounding a central core of BP230 molecules. In skin cross-sections, hemidesmosomes of variable sizes could be distinguished with BP230 and plectin occupying a position in between $\beta 4$ integrin and BP180, and the intermediate filament system. In conclusion, our data provide a detailed view of the molecular architecture of hemidesmosomes in cultured keratinocytes and skin.

KEY WORDS: Super-resolution fluorescence microscopy, Keratinocyte, Hemidesmosome, Keratin filaments, Image analysis

INTRODUCTION

Classic type-I hemidesmosomes are rivet-like structures, which play a crucial role in maintaining tissue integrity and resisting mechanical force (Walko et al., 2015). At the ultrastructural level, they appear as electron-dense plaques present on the cytoplasmic side of the plasma membrane, to which keratin intermediate filaments are anchored. At the core of each hemidesmosome is the $\alpha 6 \beta 4$ integrin, a receptor for laminin-332 (which comprises the $\alpha 3$, $\beta 3$ and $\gamma 2$ chains of laminin) in the epidermal basement membrane that binds to the intermediate filament anchoring protein plectin (Borradori and Sonnenberg, 1999). Two other components of type-I hemidesmosomes are the bullous pemphigoid antigens BP180 (collagen type XVII, BPAG2, encoded by *COL17A1*) and BP230 (BPAG1e, an epithelial splice variant of dystonin). A second type of hemidesmosome (type II), present in simple epithelia

and many cultured cells, lacks the bullous pemphigoid antigens; it contains only plectin and $\alpha 6 \beta 4$ integrin (Litjens et al., 2006).

A model for the spatial organization of hemidesmosome components has been proposed in which the two transmembrane proteins $\alpha 6 \beta 4$ integrin and BP180 are connected through plectin and BP230 to the intermediate filament system (Koster et al., 2003, 2004). However, it is unknown how the different hemidesmosome components are spatially organized relative to one another. Neither is it known how the keratin intermediate filaments are anchored to hemidesmosomes in cultured keratinocytes, or whether they are directly involved in the organization of the hemidesmosome structure (Song et al., 2015; Seltnann et al., 2015).

Here, we have used two- and three-color ground-state depletion followed by individual molecule return microscopy (GSDIM) (Hell, 2007) and quantitative image analysis to characterize in detail the architecture of nascent hemidesmosome in cultured keratinocytes. Additionally, we have applied GSDIM in the study of hemidesmosomes in tissue sections of human skin.

RESULTS AND DISCUSSION

Plectin and $\beta 4$ integrin are localized alongside keratin filaments

Studies on the role of keratin filaments in the organization of hemidesmosomes at the periphery of keratinocytes, where the assembly of filaments is initiated, have been hampered by the limited resolution of immunofluorescence microscopy. Super-resolution microscopy analyses of human keratinocytes have revealed that the keratin-14 organization at the cell periphery differs considerably from that in the more central parts (Fig. S1A). Thick keratin filament bundles occur in the center of the cell, whereas an elaborate network of fine keratin filaments running close and parallel to the basal membrane is present at the cell periphery.

To visualize keratin filaments together with either plectin or $\beta 4$ integrin, we optimized imaging conditions and introduced precise correction algorithms for acquisition of two or three very high-quality color channels from the same cell (see Materials and Methods; Fig. S1B,C). The results showed that $\beta 4$ integrin, detected using a monoclonal antibody against its extracellular domain, was closely associated with keratin filaments. But rather than overlapping, $\beta 4$ integrin was found along the keratin filaments that ran parallel to the plasma membrane (Fig. 1A). In line with the notion that keratin filaments loop through hemidesmosome plaques, they do not stop at sites where integrin $\beta 4$ is present, but rather connect these molecules while extending farther into the cytoplasm and along the plasma membrane.

Quantification of the spatial relationship between these two proteins with conventional colocalization analysis, using Pearson or Manders coefficients, for example, cannot be applied to the super-resolution images. We therefore developed alternative measures and ImageJ software routines to quantify protein–protein proximity at the

¹Division of Cell Biology, The Netherlands Cancer Institute, Plesmanlaan 121, Amsterdam 1066 CX, The Netherlands. ²Van Leeuwenhoek Centre for Advanced Microscopy, Swammerdam Institute for Life Sciences, University of Amsterdam, Amsterdam 1098 XH, The Netherlands.

*Author for correspondence (a.sonnenberg@nki.nl; k.jalink@nki.nl)

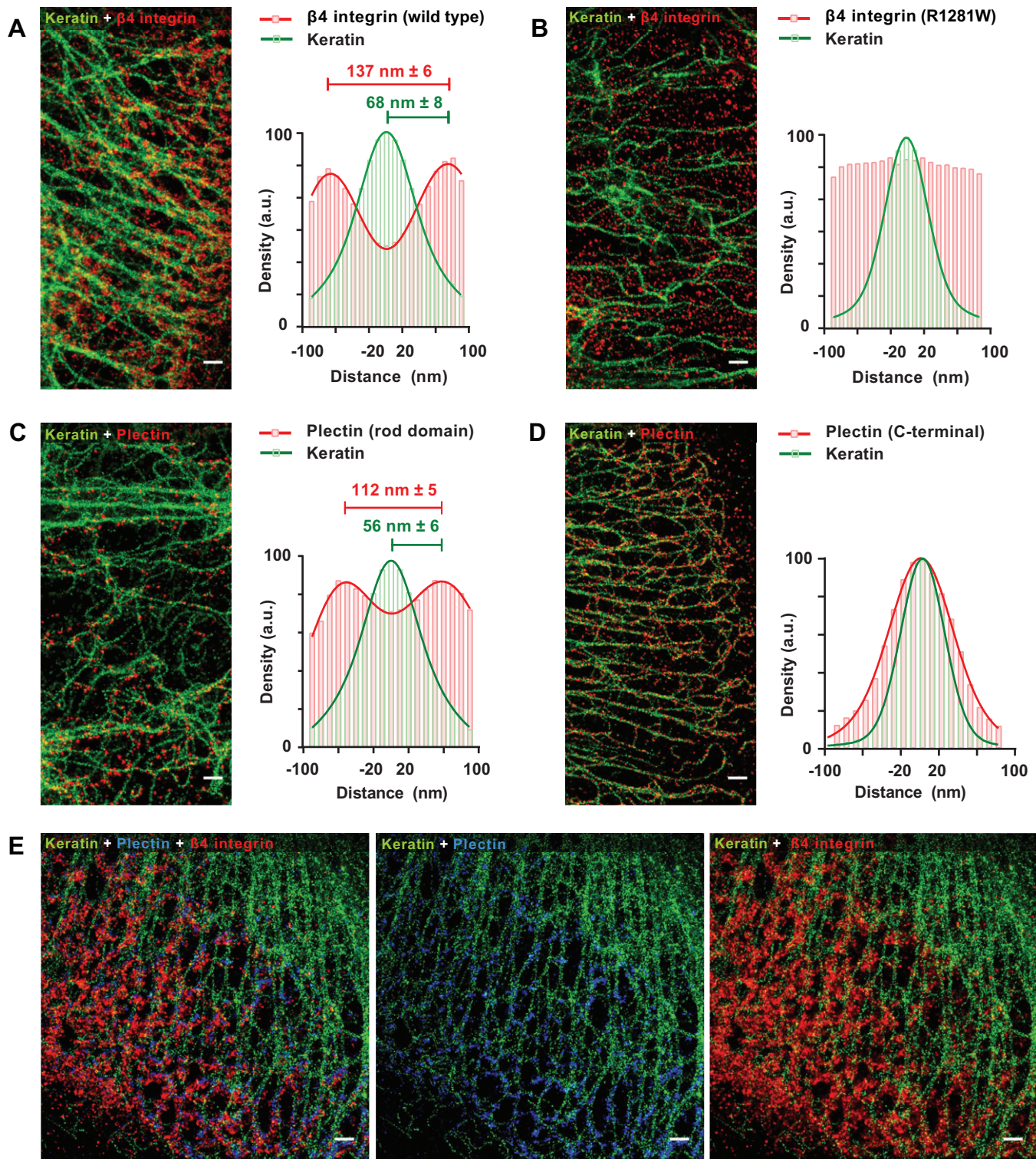


Fig. 1. Super-resolution images of keratin, $\beta 4$ integrin and plectin in cultured keratinocytes. (A) Super-resolution image of $\beta 4$ integrin and keratin-14 (left). Graphs show the average distance distribution between $\beta 4$ integrin and keratin for $n=283$ ROIs taken from 30 cells (right). Further details on image analysis are presented in Fig. S2. (B) Super-resolution image (left) and distance distribution (right) for keratin-14 and a $\beta 4$ -integrin mutant ($\beta 4^{R1281W}$ integrin) that is unable to bind to plectin. Data are averages of 109 ROIs in 10 cells. (C) Super-resolution image (left) and distance distribution (right) for keratin-14 and plectin (rod domain). Data are averages of 98 ROIs in 10 cells. (D) Super-resolution image (left) and distance distribution (right) for keratin-14 and the keratin-binding C-terminus of plectin. The overlap in localizations confirms that the plectin C-terminus interacts with keratin-14. Data are averages from 100 ROIs taken from 15 cells. (E) Three-color super-resolution imaging illustrating that plectin (rod domain) and $\beta 4$ integrin (extracellular domain) decorate keratin-14 filaments in similar patterns. Scale bars: 500 nm.

nanometer scale (Fig. 1A; Fig. S2). We determined the distribution of orthogonal distances between $\beta 4$ integrin and keratin-14 by first manually delineating single keratin filaments. Regions of interest

(ROI) containing these filaments were cut to smaller images, and the delineated filaments (splines) with associated $\beta 4$ integrin were straightened by using affine transformation, a procedure that

preserves molecular distances (Fig. S2). The graph in Fig. 1A shows the distribution of distances between $\beta 4$ integrin and the filament present in 120 ROIs. This analysis revealed that most $\beta 4$ integrin was indeed distributed alongside, rather than under, the keratin filaments, with an average distance of 68 ± 8 nm to the axis of the keratin filament (Fig. 1A; Fig. S3). By contrast, a $\beta 4$ integrin mutant that is unable to bind to plectin [$\beta 4^{R1281W}$ integrin, in which arginine at position 1281 has been replaced by tryptophan (Geerts et al., 1999)] was found to be equally distributed under and along keratin filaments (Fig. 1B; Fig. S4).

We next visualized the localization of the cytolinker plectin using a monoclonal antibody against the central rod domain. Like $\beta 4$ integrin, plectin was co-distributed with keratin filaments (Fig. 1C) and excluded, at least partially, from the area immediately under the filaments. The mean distance between the rod domain of plectin and the keratin filament (Fig. 1C, graph) was smaller than that between the extracellular domain of integrin $\beta 4$ and keratin filaments

(56 ± 6 nm vs 68 ± 8 nm). In the cells expressing $\beta 4^{R1281W}$ integrin, the rod domain of plectin appeared to be more closely localized to the keratin filaments (Fig. S4), indicating that the distance between plectin and the keratin filaments is influenced by its binding to $\beta 4$ integrin. As expected, an antibody directed against the plectin C-terminus localized closer to keratin, as determined from the overlap in the distance distributions (Fig. 1D; Fig. S3). Three-color super-resolution imaging for keratin-14, $\beta 4$ integrin and plectin confirmed that $\beta 4$ integrin and plectin were co-distributed with keratin filaments (Fig. 1D).

Thus, our microscopy findings provide the first direct confirmation that plectin interacts simultaneously and asymmetrically with $\beta 4$ integrin and keratin – i.e. the N-terminus binds to $\beta 4$ integrin while the C-terminus associates with keratin (Geerts et al., 1999; Nikolic et al., 1996). Furthermore, they underscore the importance of keratin filaments in orchestrating the assembly of hemidesmosomes (Seltmann et al., 2013).

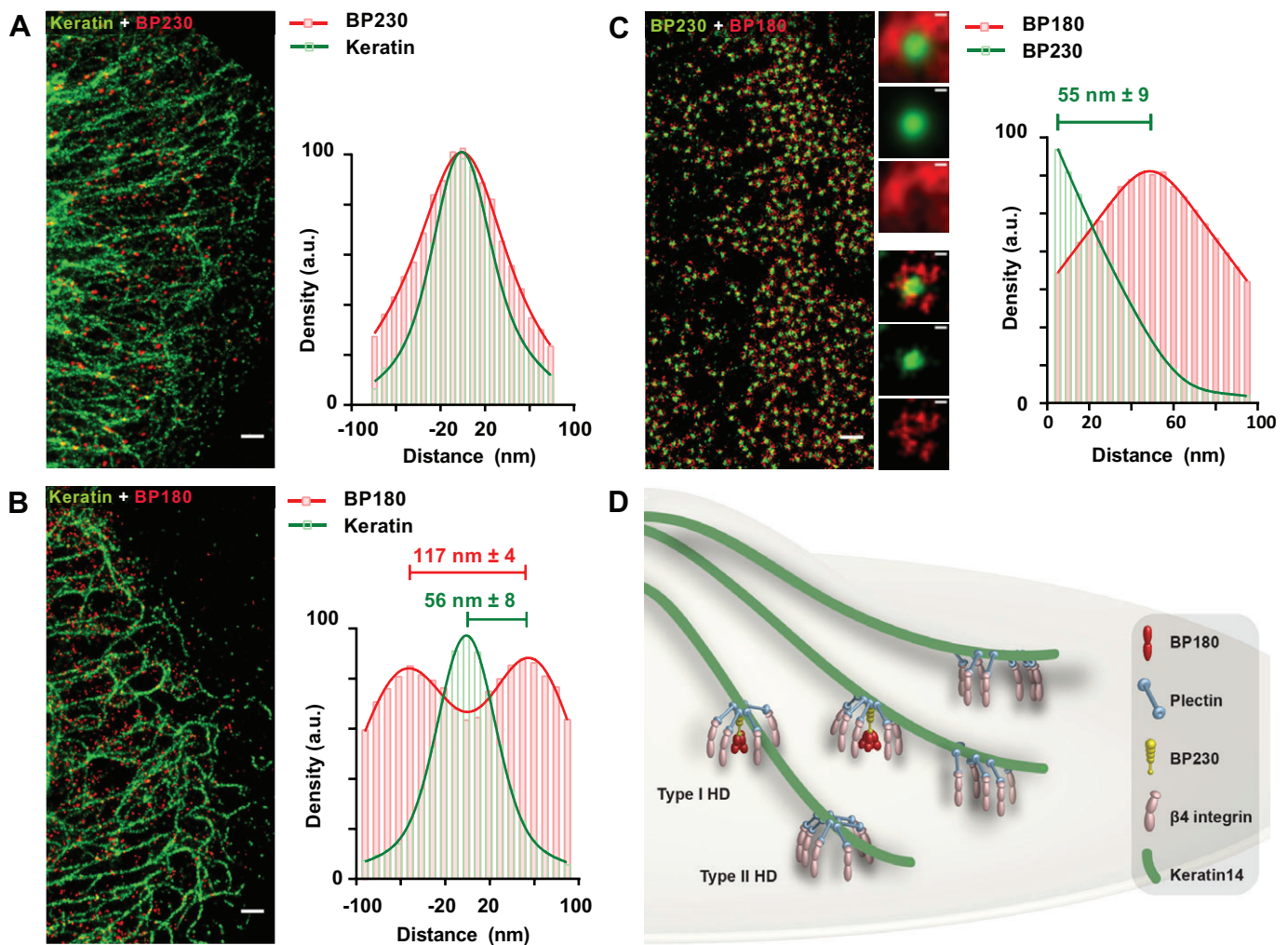


Fig. 2. Keratin, BP230 and BP180 location with super-resolution imaging. (A) Super-resolution image of BP230 (intermediate-filament-binding domain) and keratin-14. The distance distributions of keratin-14 and BP230 show that both labels overlap considerably. Data are from 93 ROIs in 11 cells. (B) Super-resolution image of BP180 and keratin-14, and distance distribution showing that BP180 is partly present alongside the filaments, yet significant overlap also occurs. Data are from 172 ROIs in 14 cells. (C) Super-resolution image of BP230 and BP180 showing dense punctae of BP230 surrounded by BP180. A region with relatively sparse labeling was selected to allow resolution of separate complexes. The magnification images depict a single type-I hemidesmosome (lower three panels) and an average projection of 53 hemidesmosomes (top three panels). For details, see the text and Fig. S2B. (Right) Distribution of the molecular distances between BP180 and BP230. (D) Drawing showing three-dimensional model for type-I and type-II hemidesmosomes. In type-I hemidesmosomes, small circular clusters of BP180 molecules are closely linked to keratin filaments through BP230. $\beta 4$ integrin is anchored to filaments through plectin in a 'tent-and-peg' model. Type-II hemidesmosomes, formed at the outermost region of the cell, only comprise $\beta 4$ integrin and plectin. Scale bars: 500 nm (A,B,C); 100 nm (magnification images in C).

Distribution of BP230 and BP180 in hemidesmosomes

Next, we examined the spatial distribution of BP180 and BP230 with super-resolution microscopy and proximity analysis. A close association between the C-terminus of BP230 and keratin-14 was observed in super-resolution images (Fig. 2A). By contrast, BP180, detected with an antibody against its extracellular domain, was located farther from the keratin filaments. It displayed a wider, bimodal distribution with a typical distance of about 56 nm (Fig. 2B). This distance is less than that between the cytoplasmic domain of $\beta 4$ integrin and keratin (68 nm, see Fig. 1A), perhaps reflecting the difference in size between plectin and BP230. Taken together, these observations corroborate the notion that the C-terminus of BP230 mediates binding to keratin.

Imaging of immunolabeled BP180 and BP230 together revealed a remarkable pattern in the distribution of the two molecules. BP230 was often observed to form bright punctae, which are almost invariably surrounded by BP180 molecules, seemingly at a regular and characteristic distance (Fig. 2C). This was particularly apparent

in areas where the molecules were relatively sparse (Fig. 2C), whereas in more dense regions, the labeling of BP180 became somewhat continuous, in stripes that appeared to follow the filaments (data not shown). Analyses of (radial) distance distributions in sparsely stained regions (Fig. S2) indicated an average distance of 55 nm between BP180 and the center of the BP230 punctae. In summary, our data indicate that BP180 and BP230 are assembled into highly organized concentric structures that are distinct from those of $\beta 4$ integrin and plectin.

BP180 and BP230 co-distribute with $\beta 4$ integrin and plectin in hemidesmosomes

The distribution of BP180 and BP230 relative to $\beta 4$ integrin and plectin in type-I hemidesmosomes was determined using antibodies against the extracellular domains of both BP180 and $\beta 4$ integrin. The results show that in the stripe-like structures that were co-distributed with keratin filaments (Figs 1 and 2), the two transmembrane proteins were in close proximity of each other

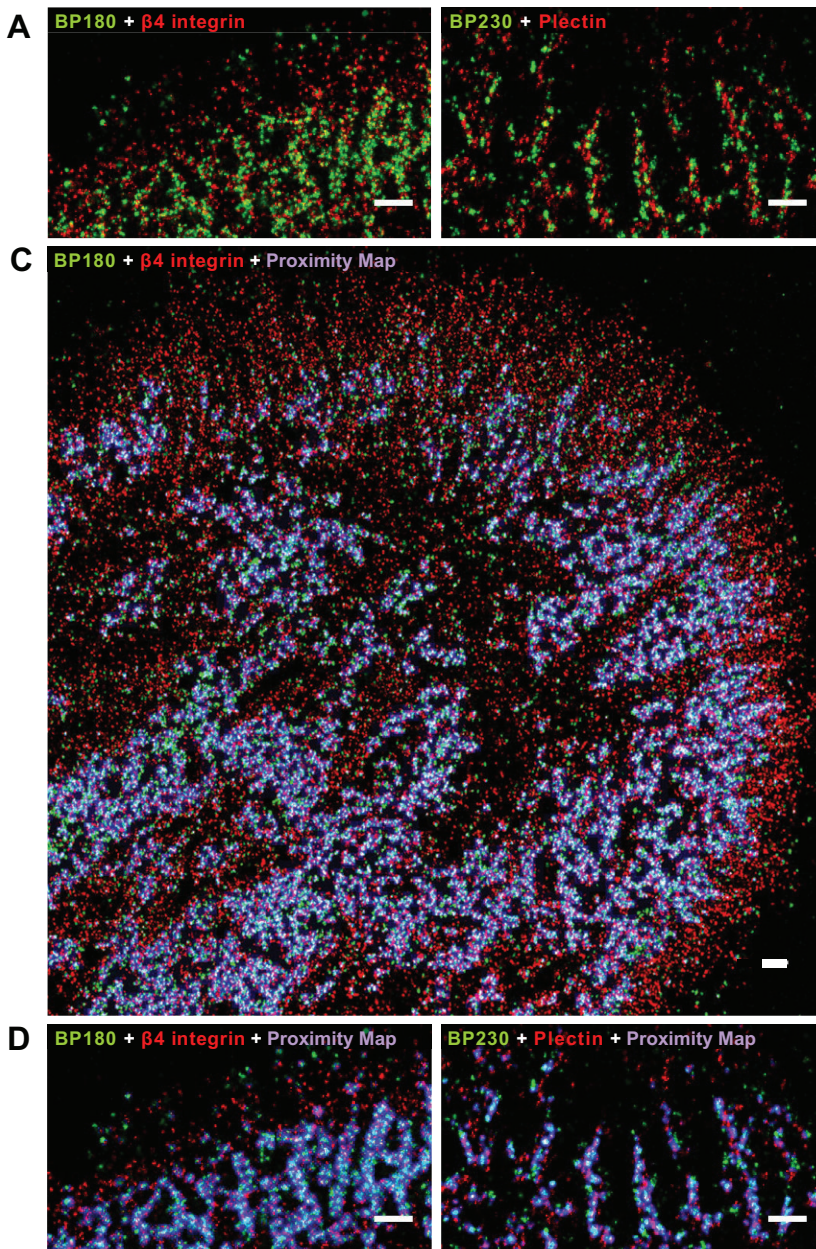


Fig. 3. Proximity mapping of hemidesmosome components in keratinocytes. (A) In keratinocytes, labeled BP180 and $\beta 4$ integrin often appear in stripes but also as individual dots. Note the appearance of single BP180 dots at the very edge of the cell and a region with predominant labeling of $\beta 4$ integrin adjacent to it. Stripe-like structures decorated with both labels are found about 1 μ m farther inwards. (B) Stripe-like localization of BP230 and plectin is visible at some distance from the cell margin but not at the cell edge. (C) Proximity map of BP180 and $\beta 4$ integrin. The intensity of blue throughout the cell denotes the prevalence of small molecular distances (<70 nm) between the two labels. Stripe-like blue areas of close proximity are not present in the outermost area ($\sim 1 \mu$ m). As in B, single BP180 molecules are present at the outermost region of the cell, and $\beta 4$ integrin occupies a small zone of $\sim 1 \mu$ m adjacent to it. The lack of blue coloration shows that the distance between these two molecules is more than 70 nm. (D,E) Detailed proximity maps of the regions depicted in A and C. Note that the blue bands in E are slightly narrower than those in D, reflecting a shorter distance between the cytolinker protein and keratin filaments. Representative images of three to five experiments are shown. Scale bars: 500 nm.

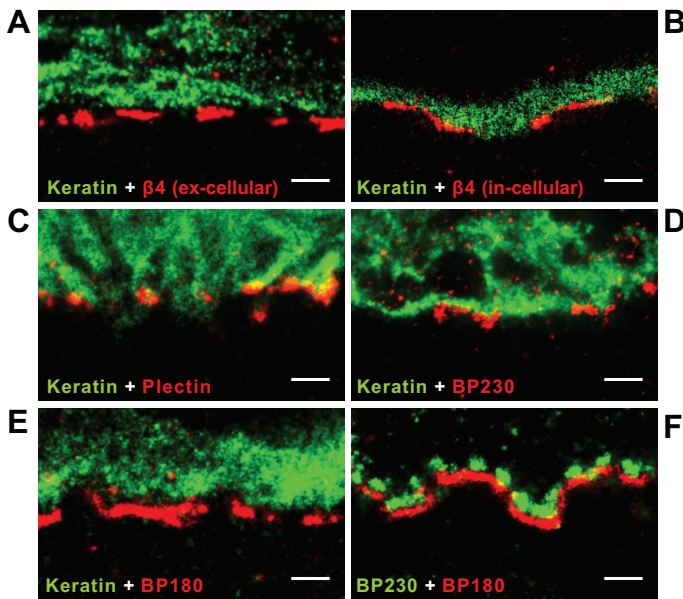


Fig. 4. Super-resolution imaging of hemidesmosome components in human skin sections. (A) Cross section of human skin tissue. The distribution of $\beta 4$ integrin (extracellular domain) and keratin-14 shows a distinct gap of 50–150 nm, which is likely to reflect the space occupied by the cytolinker plectin. (B) The labels of keratin-14 and the cytoplasmic domain of $\beta 4$ integrin are juxtaposed but do not overlap. (C) Keratin-14 and plectin (rod domain) labels partially overlap and show no visible gap. (D) The BP230 label partially overlaps with that of keratin-14 with no discernable gap. (E) A gap of about 100–150 nm is also visible between keratin and BP180. (F) Individual hemidesmosomes resolved with super-resolution imaging in human skin. As *in vitro*, in skin sections, BP230 appears punctate and surrounded by patches of BP180. All images are representatives of at least five different preparations. Scale bars: 500 nm.

(Fig. 3A). More towards the periphery of the cell, there was a region in which $\beta 4$ integrin occurred without labeling of BP180, whereas at the very front of the cell, some isolated BP180 was present. BP230 and plectin, detected with antibodies against their C-terminals, appeared to be closer to each other, in line with their direct interaction with keratin filaments (Fig. 3B).

To quantify these observations, we developed an automatic image analysis method for mapping protein proximity in super-resolution images (Fig. S2C). Molecular proximity was visualized by using false-color (blue) superposition, the intensity of which decreases with increasing distance between the red and green labels. In the proximity map in Fig. 3C, the spots with an intense blue color indicate that BP180 and $\beta 4$ integrin were not distributed in a mutually exclusive manner, but rather were localized together over large areas of the cell. No specific proximity was detected between $\beta 4$ integrin and an unrelated membrane protein, MHC class 1 heavy chain (not shown). In these analyses, proximity cut-off was set at 70 nm. Importantly, there was no tight association between the two molecules in the outermost region of the cell periphery (Fig. 3D). Proximity mapping of BP230 and plectin (Fig. 3E) yielded a narrower blue-striped structure, indicating that they were in close apposition to keratin filaments. The filamentous patterns for the different pairs of hemidesmosome components in the proximity maps provide further support for a role of keratin in the organization of hemidesmosomes in cultured keratinocytes (Figs 2 and 3).

In conclusion, proximity mapping shows that BP180 and $\beta 4$ integrin are not distributed in an alternating or random manner, but co-distribute in large regions of the cells (Fig. 3C–E). The data support a model in which nascent hemidesmosomes, formed at the outer zone of the cell, mature in the more central parts of

the cell through the recruitment of BP230 and BP180 (Koster et al., 2004).

Super-resolution fluorescence microscopy of hemidesmosome components in skin

To investigate and compare the molecular organization of hemidesmosomes in cultured keratinocytes with that in tissues, we performed super-resolution fluorescence microscopy on cross-sections of human skin. Antibodies against the extracellular domain of $\beta 4$ integrin produced a discontinuous linear staining pattern along the base of the keratinocytes, whereas antibodies against keratin-14 apparently reacted with an irregular and dense network of keratin filaments in the cytoplasm (Fig. 4A). Strikingly, there was a visible gap of 50–150 nm between the two labels that is likely to reflect the space occupied by plectin and the intracellular part of $\beta 4$ integrin. The gap was detectably smaller when an antibody against the $\beta 4$ integrin cytoplasmic domain was used (Fig. 4B). Furthermore, sections labeled with antibodies against the central rod domain (Fig. 4C) or the C-terminal keratin-binding domain of plectin (data not shown) showed a close proximity of keratin and plectin with little, if any, discernible space between them. Staining for BP180 (cytoplasmic domain) and BP230 (C-terminal domain) revealed that, in skin sections, BP230 was also in close proximity to keratin filaments (Fig. 4D), whereas there was a gap of 100–150 nm between BP180 and keratin (Fig. 4E). We also often found BP230 in distinct punctae at the basal membrane (Fig. 4D,F). These results illustrate that the architecture of hemidesmosome in skin, with the cytolinkers plectin and BP230 linking keratin filaments to the transmembrane proteins $\beta 4$ integrin and BP180, resembles that observed in cultured keratinocytes.

In summary, we have mapped the position of proteins in hemidesmosomes in unprecedented detail by using super-resolution microscopy and proximity analysis, and for the first time show that formed hemidesmosomes in the peripheral parts of cultured keratinocytes are associated with keratin filaments, and that BP180 and BP230 have a characteristic arrangement within hemidesmosomes.

MATERIALS AND METHODS

Antibodies

The following antibodies were used: anti-keratin-14 (Covance), 121 (against the rod domain of plectin; Hieda et al., 1992), 233 (against the cytoplasmic domain of BP180; Nishizawa et al., 1993), 439-9B (against the extracellular domain of $\beta 4$ integrin), 450-11A (against the cytoplasmic domain of $\beta 4$ integrin), 5E (against the C-terminal domain of BP230; Ishiko et al., 1993), P1 (against the C-terminal plakin-repeat of plectin; Stegh et al., 2000) and anti-BP230 (recognizing the C-terminal domain of BP230; Tanaka et al., 1990). Secondary goat antibodies were: anti-rat IgG (Alexa-Fluor-488- or Alexa-Fluor-647-conjugated), anti-rabbit IgG (Alexa-Fluor-488-, Alexa-Fluor-532- or Alexa-Fluor-647-conjugated), anti-mouse IgG (Alexa-Fluor-488-, Alexa-Fluor-532- or Alexa-Fluor-647-conjugated), anti-guinea pig IgG (Alexa-Fluor-488-conjugated) and anti-human IgG (Alexa-Fluor-488-conjugated) from Invitrogen.

Cell lines and immunofluorescent analysis

Pyloric atresia junctional epidermolysis bullosa (PA-JEB) keratinocyte cells expressing $\beta 4$ integrin (PA-JEB/ $\beta 4$) or $\beta 4^{R12181W}$ integrin (PA-JEB/ $\beta 4^{R12181W}$) were cultured as described previously (Geerts et al., 1999). For immunofluorescent analysis, keratinocytes grown on coverslips were fixed, permeabilized and incubated with primary and secondary antibodies at room temperature with extensive washing steps in between.

Sections (~5 μ m thick) of skin frozen in optimal cutting temperature (OCT) compound were placed onto coverslips coated with 10% poly-L-lysine and dried for 1 h at room temperature. After washing with PBS for

5 min, sections were fixed in 2% paraformaldehyde for 10 min, blocked with 2% BSA in PBS and incubated with primary and secondary antibodies as described above.

Optimized super-resolution imaging

Super-resolution microscopy in total internal reflection fluorescence (TIRF) or epifluorescence mode was performed with a Leica SR-GSD microscope (Leica Microsystems) equipped with 488-, 532- and 647-nm lasers, using a 160× oil immersion objective and, for three-dimensional images, an astigmatic lens. Much effort was dedicated towards optimization of two- and three-color image acquisition as well as to post-acquisition corrections. A full description is given in Fig. S1B,C and the legend. Full super-resolution versions of figures 1 to 4 can be downloaded at <https://icedrive.nki.nl/sharedcontent.aspx?s=499C179995B0B10DC8F85E90D44953E400F53EFC> or obtained from K. Jalink by email request.

Acknowledgements

We are grateful to K. Owaribe, H. Herrmann, J. R. Stanley and T. Hashimoto for reagents; and A. Carisay and A. Agronskaya for assistance with ThunderSTORM software and image corrections, respectively.

Competing interests

The authors declare no competing or financial interests.

Author contributions

K.J. and A.S. conceived and designed the experiments; L.N., M.K. and P.S. performed experiments; L.N., B.v.d.B., P.S.; A.S. and K.J. analyzed the data; L.N., B.v.d.B., E.M.M.M. and K.J. optimized super-resolution microscopy; and L.N., K.J. and A.S. wrote the manuscript.

Funding

This work was supported by STW (to K.J.); and the Dutch Cancer Society (to A.S.).

Supplementary information

Supplementary information available online at <http://jcs.biologists.org/lookup/suppl/doi:10.1242/jcs.171892/-/DC1>

References

- Borradori, L. and Sonnenberg, A. (1999). Structure and function of hemidesmosomes: more than simple adhesion complexes. *J. Invest. Dermatol.* **112**, 411–418.
- Geerts, D., Fontao, L., Nievers, M. G., Schaapveld, R. Q. J., Purkis, P. E., Wheeler, G. N., Lane, E. B., Leigh, I. M. and Sonnenberg, A. (1999). Binding of integrin $\alpha 6 \beta 4$ to plectin prevents plectin association with F-actin but does not interfere with intermediate filament binding. *J. Cell Biol.* **147**, 417–434.
- Hell, S. W. (2007). Far-field optical nanoscopy. *Science* **316**, 1153–1158.
- Hieda, Y., Nishizawa, Y., Uematsu, J. and Owaribe, K. (1992). Identification of a new hemidesmosomal protein, HD1: a major, high molecular mass component of isolated hemidesmosomes. *J. Cell Biol.* **116**, 1497–1506.
- Ishiko, A., Shimizu, H., Kikuchi, A., Ebihara, T., Hashimoto, T. and Nishikawa, T. (1993). Human autoantibodies against the 230-kD bullous pemphigoid antigen (BPAG1) bind only to the intracellular domain of the hemidesmosome, whereas those against the 180-kD bullous pemphigoid antigen (BPAG2) bind along the plasma membrane of the hemidesmosome in normal human and swine skin. *J. Clin. Invest.* **91**, 1608–1615.
- Koster, J., Geerts, D., Favre, B., Borradori, L. and Sonnenberg, A. (2003). Analysis of the interactions between BP180, BP230, plectin and the integrin $\alpha 6 \beta 4$ important for hemidesmosome assembly. *J. Cell Sci.* **116**, 387–399.
- Koster, J., van Wilpe, S., Kuikman, I., Litjens, S. H. M. and Sonnenberg, A. (2004). Role of binding of plectin to the integrin $\beta 4$ subunit in the assembly of hemidesmosomes. *Mol. Biol. Cell* **15**, 1211–1223.
- Litjens, S. H. M., de Pereda, J. M. and Sonnenberg, A. (2006). Current insights into the formation and breakdown of hemidesmosomes. *Trends Cell Biol.* **16**, 376–383.
- Nikolic, B., Mac Nulty, E., Mir, B. and Wiche, G. (1996). Basic amino acid residue cluster within nuclear targeting sequence motif is essential for cytoplasmic plectin-vimentin network junctions. *J. Cell Biol.* **134**, 1455–1467.
- Nishizawa, Y., Uematsu, J. and Owaribe, K. (1993). HD4, a 180 kDa bullous pemphigoid antigen, is a major transmembrane glycoprotein of the hemidesmosome. *J. Biochem.* **113**, 493–501.
- Seltmann, K., Roth, W., Kröger, C., Loschke, F., Lederer, M., Hüttelmaier, S. and Magin, T. M. (2013). Keratins mediate localization of hemidesmosomes and repress cell motility. *J. Invest. Dermatol.* **133**, 181–190.
- Seltmann, K., Cheng, F., Wiche, G., Eriksson, J. E. and Magin, T. (2015). Keratins stabilize hemidesmosomes through regulation of $\beta 4$ -integrin turnover. *J. Invest. Dermatol.* **135**, 1609–1620.
- Song, J.-G., Kostan, J., Drepper, F., Knapp, B., de Almeida Ribeiro, E., Jr., Konarev, P. V., Grishkovskaya, I., Wiche, G., Gregor, M., Svergun, D. I. et al. (2015). Structural insights into Ca^{2+} -calmodulin regulation of plectin 1a-integrin $\beta 4$ interaction in hemidesmosomes. *Structure* **23**, 558–570.
- Stegh, A. H., Herrmann, H., Lampel, S., Weisenberger, D., Andra, K., Seper, M., Wiche, G., Krammer, P. H. and Peter, M. E. (2000). Identification of the cytolinker plectin as a major early in vivo substrate for caspase 8 during CD95- and tumor necrosis factor receptor-mediated apoptosis. *Mol. Cell Biol.* **20**, 5665–5679.
- Tanaka, T., Korman, N. J., Shimizu, H., Eady, R. A. J., Klaus-Kovtun, V., Cehrs, K. and Stanley, J. R. (1990). Production of rabbit antibodies against carboxy-terminal epitopes encoded by bullous pemphigoid cDNA. *J. Invest. Dermatol.* **94**, 617–623.
- Wallo, G., Castañón, M. J. and Wiche, G. (2015). Molecular architecture and function of the hemidesmosome. *Cell Tissue Res.* **360**, 529–544.



Special Issue on 3D Cell Biology

Call for papers

Submission deadline: January 16th, 2016

Journal of Cell Science

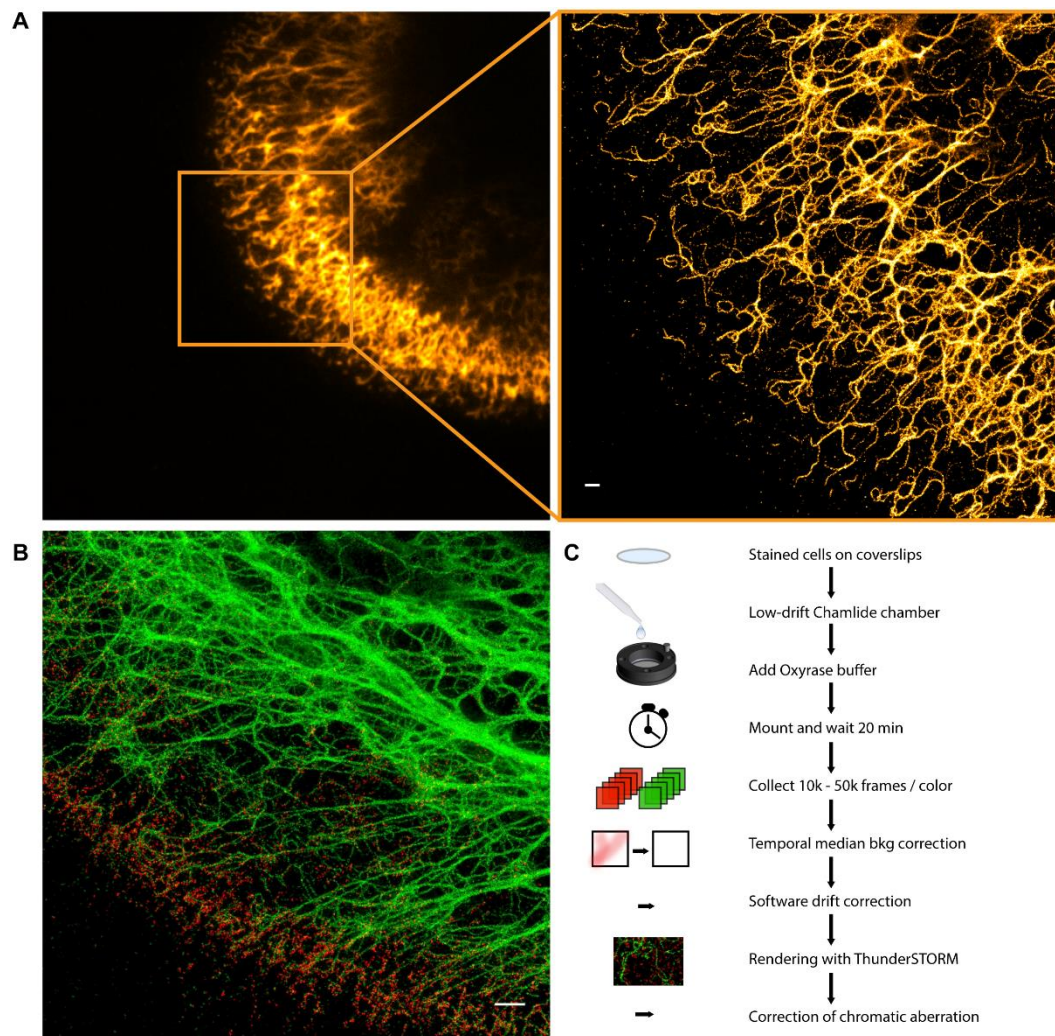


Figure S1. Imaging the fine keratin filament network in the periphery of the cell.

(A) Keratin filaments observed by TIRF (left) and SR microscopy (right). The SR image shows individual filaments running parallel to the basal membrane. The filaments in the outer rim of the cell are thinner in diameter. Scale bar: 500 nm. (B) Optimized two-color SR image of keratin and plectin. Scale bar: 500 nm. (C) Schematic overview of the various optimized acquisition and correction steps to obtain the highly-corrected two- and three-color GSD images in this paper.

Coverslips with stained cells were mounted in a Chamblide CMB magnetic chamber (Live Cell Instrument, Seoul, South Korea). Of several commercial dishes and holders, the Chamblide holders were found to have minimal drift, as detected by analyzing long time-lapse image series taken from coverslips with sparse sub-resolution fluorescent beads (Invitrogen). Popular imaging buffers for SR microscopy are typically optimal only for a single channel (fluorescent dye). Since physicochemical blinking mechanisms may vary widely between different dyes, the fluorophores in extra channels (second- and third colors) show suboptimal blinking kinetics and brightness, leading to significantly diminished image quality in these channels. We tested several alternative buffer formulations, aiming specifically to optimize blinking for two- and three-dye SR imaging and thereby obtain high quality multi-color images.

These tests resulted in a new oxygen scavenging buffer, termed OXEA (a mixture of mercaptoethylamine (50 mM), the oxygen scavenger system Oxyrase (OXYRASE Inc, Mansfield, Ohio, USA, 3%) and sodium-L-lactate (12%, w/w) in PBS). We found that this buffer supports fast and bright blinking of Alexa Fluor-647, AF-488 and AF-532 for two- and three-color imaging (full details to be published elsewhere). After addition of 500 μ l of OXEA to the coverslips, cells were mounted on the microscope and the preparation was left to stabilize for 15-30 min to avoid initial drift before SR data were acquired. A total of 10.000 to 50.000 frames (10 ms) were collected for each channel. Blinking detection threshold was set at 70 photons/pixel (~500 photons/event). For 2-color imaging, the Alexa-647 channel was imaged first, followed by Alexa-488. These two dyes show essentially no leak-through. For 3-color SR imaging, we first imaged Alexa-647, followed by Alexa-488 (with 500/30 band-pass filter to prevent leak-through of Alexa-532). Thereafter, Alexa-488 had bleached enough to prevent leak through in the third channel, Alexa-532. For post-acquisition correction steps, data were transferred to an off-line workstation. First, we applied our temporal median background correction (Hoogendoorn et al., Scientific Reports 2014) to the raw data using home-built software (available on request). This correction proved especially powerful to improve the image quality in densely labeled structures. Following that, any residual X/Y drift was removed from the data using a home-built 'de-jittering' routine. For image rendering, the Image J plugin ThunderSTORM (Ovesny et al., Bioinformatics 2014) was used with final pixel size of 10 nm and, if many events were present, additional filtering to reject the least precise localizations. Alternatively, the built-in de-jittering algorithm of recent versions of ThunderSTORM was used. As a final step, chromatic aberrations (CA) were precisely corrected. CA (of up to 60 nm) was mapped throughout the focal plane by imaging 0.1 μ m diameter Tetraspec microspheres (Invitrogen) embedded in a matrix. An affine transformation matrix was constructed from those data and affine correction of all images was carried out using a home-build ImageJ macro (available on request). CA was highly stable over several months of imaging. While elaborate, these improvements allowed us to routinely obtain very good quality two- and three-color images.

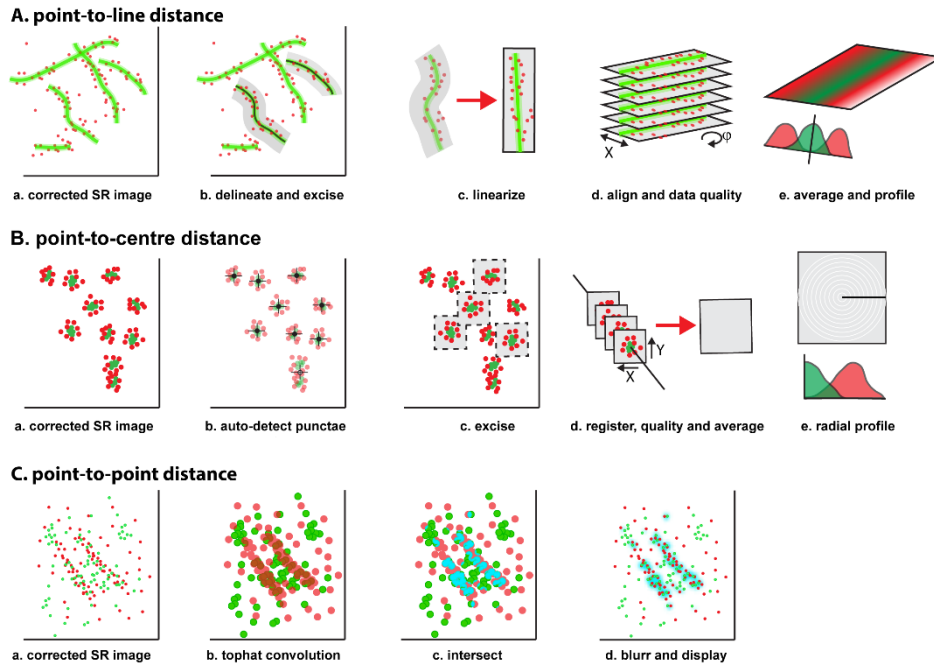


Figure S2. Calculation of molecular distance distributions and proximity mapping.

(A) Determining the distribution of distances between one label decorating a filament and an arbitrary second label. In SR images (a) containing filaments and additional label(s), the centers of individual un-branched filaments was delineated manually by drawing curved lines (b) of 500 nm width onto the keratin channel. We made sure that filaments were single-stranded and well-separated so as to avoid potential overlap with nearby filaments. Then each of the selected curved Regions Of Interest (ROI) surrounding a single filament was excised (b) and linearized (c) using the straightening (affine transformation) routine in ImageJ. This routine warps the image so as to linearize the curved lines as well as the image area surrounding it. Because radius of curvature is very large in relationship to the detected distances, this does not alter the average distances of individual points ($\beta 4$, etc.) to the linearized filaments. The straightened filaments (ROIs) were precisely oriented vertically by image rotation, divided up in shorter line segments of $\sim 1 \mu\text{m}$ long and centered laterally with sub-pixel resolution (d) by Gaussian fitting of the intensity profile of the filaments. This automated alignment procedure (macro available on request) corrects for slight inaccuracies in tracing, and it allows for data cleanup by discarding those sub-images in which the Gaussian fit does not fulfill constraints on filament width and goodness-of-fit. To calculate the distribution of distances between keratin and the second color channel (integrin $\beta 4$, plectin, BP230 or BP180) the sub-images were summed and projected onto a line orthogonal to the filament direction (e). Validity of this analysis was verified by analyzing synthetic (in silico) data sets with our routines. These tests showed that the affine transformation and alignment routines did not affect average measured distances, while only a very slight ($\sim 1 \text{ nm}$) effect was observed on the width of the distribution. (B) To detect radial distances in the circular patterns of BP230 and BP180 (a), punctae of bright staining were detected by thresholding and size-exclusion based on the BP230 channel (b), and the surrounding regions of interest (200 x 200 nm) (c) were copied into an ROI image dataset. Excised ROIs were automatically aligned with sub-pixel precision based on the center of gravity of the BP230 signal (d), and the average image of all data was constructed for both channels (d, below). The intensity-distance distribution was then made by averaging the intensities in concentric circles with indicated radii to the center of BP230 (e). (C) To produce pixel maps that visualize molecular proximity (at a user-selected scale), the two color channels (a) are convolved with a normalized 2D circular top-hat kernel of size R (b), which evenly dilates individual bright pixels over a range R while keeping the integrated intensity unchanged. On the resulting images conventional colocalization was applied using thresholding according to Costes method (Costes et al., 2004), after which local proximity was computed as ($\text{SQRT}(\text{gray value}_{\text{channel1}} \times \text{gray value}_{\text{channel2}})$) (c). This procedure thus yields a proximity map that depicts vicinity of the two colors up to a scale R . This method can be extended to show proximity in a distance r (range $0 < r < R$) by subtracting two proximity maps produced with kernel sizes R and r . By overlaying the *proximity map* with the original multicolor Super-Resolution image (d), the places in the image where the two labels are in close vicinity are clearly marked visually. As control, no significant proximity was observed between $\beta 4$ and an Ab against an unrelated membrane protein, MHC heavy chain. All data analysis was based on the nr of ROIs indicated in the text. ROIs were selected from 7-30 individual cells, and each experiment was carried out at least 5 times on separate days. Further information and software routines may be obtained by emailing k.jalink@nki.nl

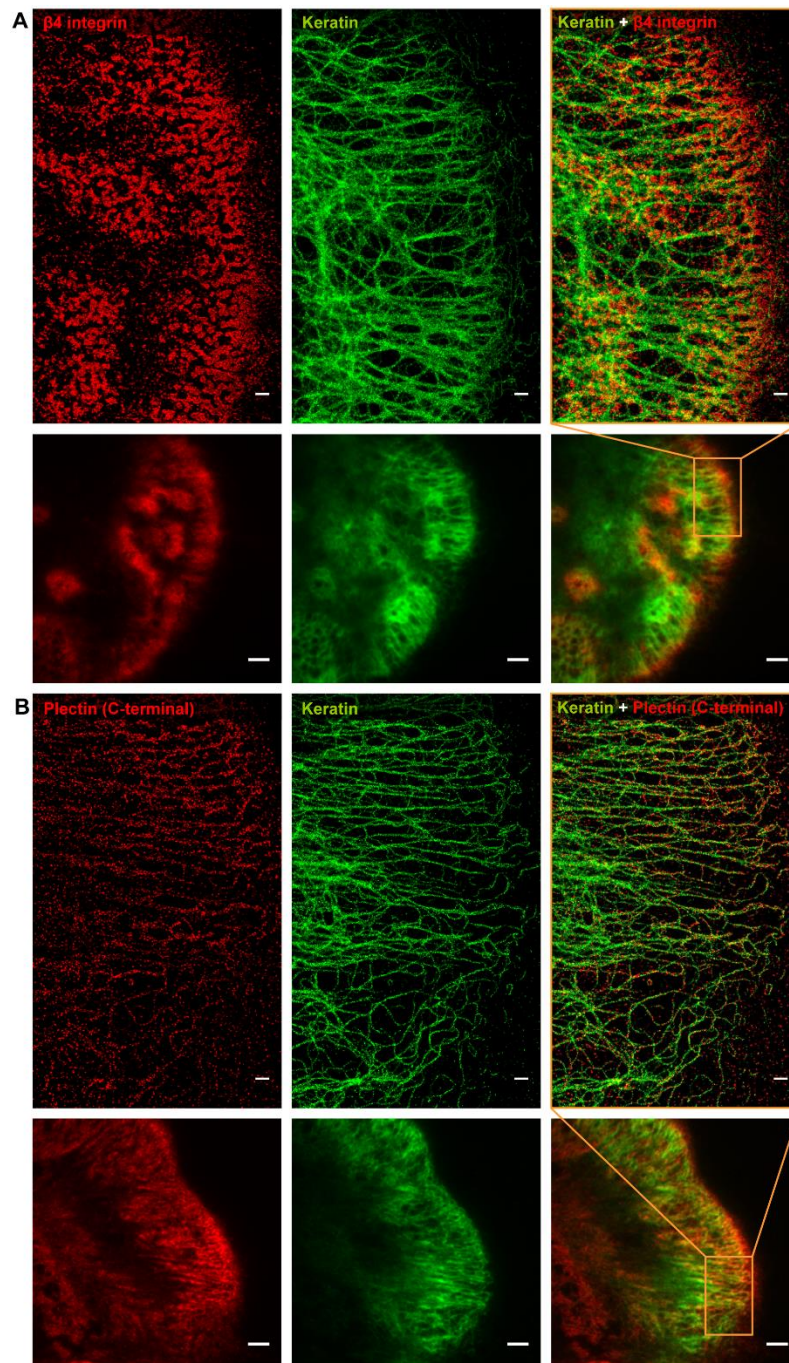


Figure S3. Comparison of the distribution of $\beta 4$ and plectin with keratin-14 in PA-JEB/ $\beta 4$ keratinocytes. Representative high-resolution images of cells stained for keratin-14 and $\beta 4$ integrin (A) or for keratin-14 and plectin (B; Ab against the C-terminus), together with the TIRF images to provide cellular context. Note that the pdf images allow zoom-in to 10 nm resolution. Scale bars are 500 nm (3 μ m for TIRF images).

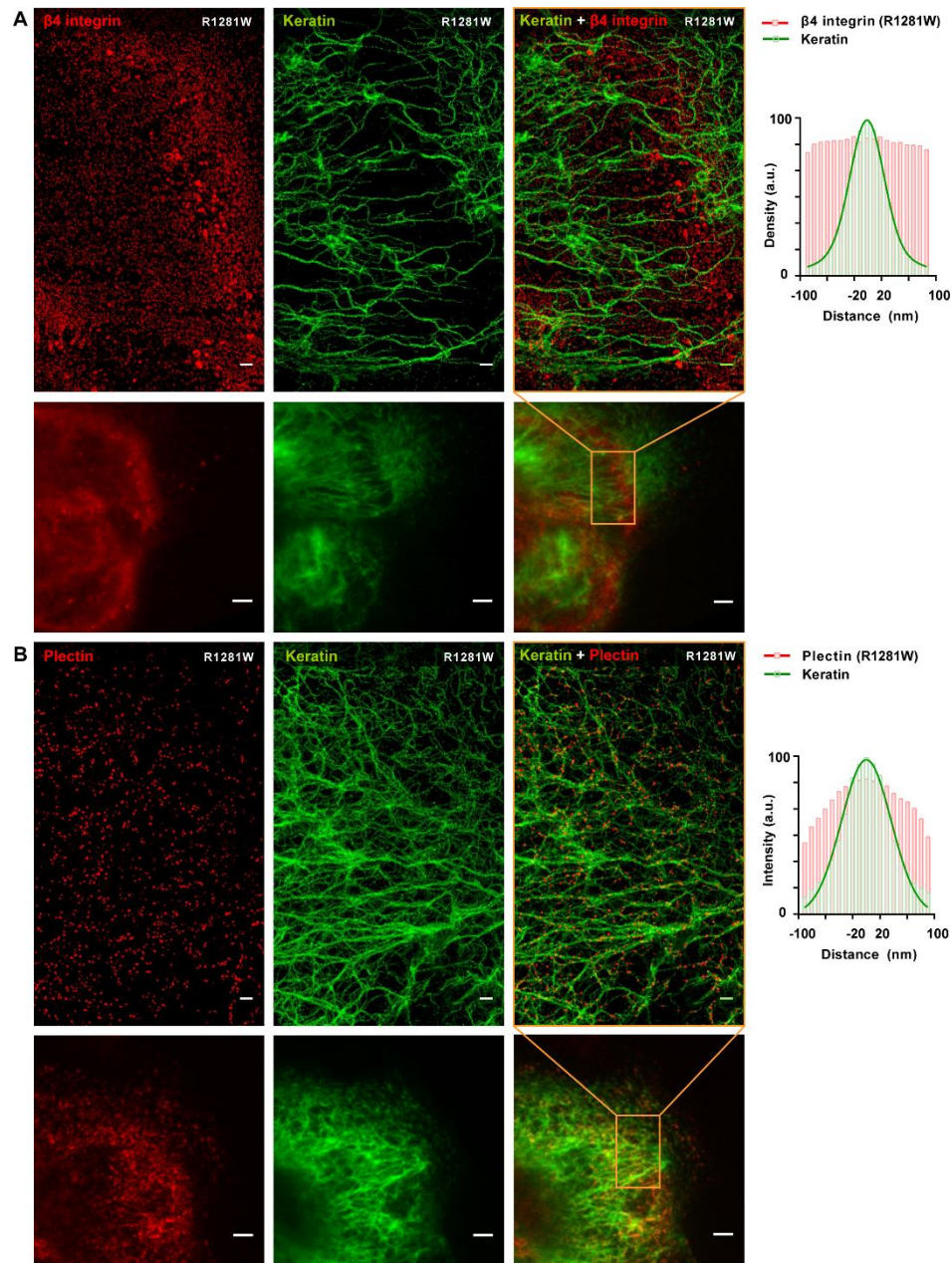


Figure S4. Comparison of the distribution of $\beta 4$ and plectin with keratin-14 in PA-JEB keratinocytes expressing $\beta 4^{R1281W}$.

(A) High-resolution and TIRF images of cells stained for keratin-14 and $\beta 4$ integrin. The graph showing the distance distribution between plectin and keratin-14 is identical to that in Fig. 1B. It illustrates that there is no specific distribution of $\beta 4$ along the keratin filaments in these cells. (B) High-resolution and TIRF images of keratin-14 and plectin (Ab against rod domain). The graphs show the distance distribution between plectin and keratin-14 in PA-JEB keratinocytes expressing mutant $\beta 4^{R1281W}$. Because the $\beta 4$ mutant cannot interact with plectin, plectin is no longer held in position along keratin filaments but is flexible. The consequent change in distribution from bi-modal (Fig. 2C; wt $\beta 4$) to unimodal ($\beta 4^{R1281W}$) supports the tent-and-peg model. Average results are shown from $n=160$ ROIs taken from $n=8$ cells. Scale bars are 500 nm (3 μ m for TIRF images).

References:

Costes, S.V., Daelemans, D., Cho, E.H., Dobbin, Z., Pavlakis, G., and Lockett, S. (2004). Automatic and quantitative measurement of protein-protein colocalization in live cells. *Biophys J.* 86, 3993-4003.

Hoogendoorn, E., Crosby, K.C., Leyton-Puig, D., Breedijk, R.M., Jalink, K., Gadella, T.W., and Postma, M. (2014). The fidelity of stochastic single-molecule super-resolution reconstructions critically depends upon robust background estimation. *Sci. Rep.* 4, 3854.

Ovesný, M., Křížek, P., Borkovec, J., Svindrych, Z., and Hagen, G.M. (2014). ThunderSTORM: a comprehensive ImageJ plug-in for PALM and STORM data analysis and super-resolution imaging. *Bioinformatics* 30, 2389-2390.